Lossless Phase Change Materials for Adjustable Tamm Plasmon Polaritons in the Near-infrared

Ming-Jyun Ye [1,2], Rashid G. Bikbaev [3,4], Pavel S. Pankin[3,4], Lu-Hsing Chen[3], David Chiu[6], Ivan V. Timofeev [3,4], Hung-Wen Chen [3], Satoshi Ishii [2], and Kuo-Ping Chen [3 *]

[1] *College of Photonics, National Yang Ming Chiao Tung University, Tainan, Taiwan*
[2]*Research Center for Materials Nanoarchitectonics (MANA), National Institute for Materials Science (NIMS), Tsukuba, Japan*
[3] *Institute of Photonics Technologies, National Tsing Hua University, Hsinchu, Taiwan*
[3]*Kirensky Institute of Physics, Federal Research Center KSC SB RAS, Krasnoyarsk 660036, Russia*
[4] *Institute of Engineering Physics and Radio electronics, Siberian Federal University, Krasnoyarsk 660041, Russia*
[6]*International Intercollegiate Ph.D. Program, National Tsing Hua University, Hsinchu 300044, Taiwan*
**kpchen@ee.nthu.edu.tw*

[*]Corresponding Author: kpchen@ee.nthu.edu.tw

ABSTRACT: Incorporating a phase-change materials (PCM) to a nanophotonic structure is a straightforward way to make it tunable. The binary semiconducting chalcogenide, antimony trisulfide (Sb_2S_3), is a suitable PCM for nanophotonic applications in the near-infrared (NIR) owing to its high refractive index, low optical losses, and wide bandgap properties. Here, the Sb_2S_3 layer is embedded between the distributed Bragg reflector (DBR) and the metal layer where Tamm plasmon polaritons (TPPs) are excited at the interface. The TPP resonance shift of 45 nm is caused by the phase change of Sb_2S_3 from amorphous to crystal. Also, the resonance shifts of 85 nm, 76 nm, and 63 nm are achieved by unpolarized, TM mode, and TE mode NIR light, respectively, depending on oblique angle incidences.

KEYWORDS: *Antimony trisulfide, distributed Bragg reflector, phase-change materials, Tamm plasmon polaritons metasurface, high refractive index*

Introduction

Optical communication has received great attentions in the recent years. Silicon and germanium photonics have been compatible with complementary metal-oxide semiconductor (CMOS) technology in photonic integrated circuits (PICs)[1 2, 3]. Variety of PIC elements have developed to manipulate light through optical couplers[3, 4], modulators[5, 6], polarization beam splitters[7, 8], and optical filters[9, 10]. Based on passive and active PIC designs, versatile elements have been developed in different areas such as flash memory[11], quantum information[12, 13], biosensor[14, 15], and electric vehicle[16]. They were called application-specific photonic integrated circuits (ASPICs)[17].

For the development of nanophotonics devices, plasmonics and metasurfaces are the two emerging research fields. However, as they typically involve complex 2D and 3D nanostructure, it is challenging for large area fabrication [18, 19]. Among the nanophotonic designs, even with a one-dimensional (1D) planar photonic, obtaining high-Q resonance is possible, known as Tamm plasmon states. The Tamm plasmonic state is one of the photonic resonances experimentally demonstrated between the distributed Bragg reflector (DBR) and a metal layer, which excites Tamm plasmon polaritons (TPPs) [20, 21]. It has electric-field solid confinement at the interface, high design wavelength resolution, and independent incidence polarization compared to surface plasmon polaritons. When researchers further explored tunable TPP devices, liquid crystals were considered to enable switchable functionality in TPP systems[22] . Even though liquid crystals are matured materials, they still have some problems with modulation speed and static power consumption in LiDAR systems or micro-scale liquid-crystal-based device[23]. Therefore, this paper proposes a nonvolatile-reconfigurable solid-state 1D nanophotonic sensor that can tune the TPP resonances in the near-infrared.

In addition to liquid crystals, phase-change materials (PCMs) have been widely applied in switchable electronics and photonics [24-28]. Typically used PCMs include vanadium dioxide (VO_2), germanium-antimony-tellurium (GST), and antimony trisulfide (Sb_2S_3). The crystal phase of VO_2 was switched from a monoclinic state near 340 K. The working system of GST was above 380 K at the communication wavelength. Moreover, these two PCMs have a high extinction coefficient of around 0.5 and 2.0 in the visible, respectively [29]. On the Contrary, a binary semiconducting chalcogenide Sb_2S_3 has a band gap of 1.8 to 2.1 eV such that the absorption band edge is in the visible. Meanwhile, the high refractive index (HRI) of Sb_2S_3 can be tuned from 3 to 4 at around 650 nm. Also, its extinction coefficient was below 0.05 longer than 700 nm in both states. The nonvolatile property of Sb_2S_3 decreases the energy consumed to keep it in its original state that satisfies the green and environmentally friendly. Therefore, Sb_2S_3 has been a good candidate for nanophotonic design in the NIR spectrum. Sreekanth reported that Sb_2S_3 and SiO_2 acted as pair layers of DBR to achieve the TPP signal for surface-enhanced Raman spectroscopy (SERS)[30]. However, we found that such an HRI refractive material was sensitive when combined with DBR. In other words, it was not easy to control the same Sb_2S_3 thickness in each pair due to its high evaporate rate, leading to unexpected wavelength variations. Therefore, in this investigation, Sb_2S_3 was used as a reconfigurable functional layer in the PC-TPP structure. After the annealing process, the modulable wavelength was demonstrated to be around 45 nm. In addition, the three types of PCM were discussed with the same sub-wavelength thickness in the PC-TPP simulation design. Moreover, the analysis of angle-dependent resonance was also proved to be about 85 nm from in NIR. It was shown that our design would support in LiDAR [31, 32], and sensor [33] applications.

RESULTS AND DISCUSSION

The optical constant of three phase change materials (Sb_2S_3, VO_2, and GST) were shown in Figure 1. See Figure 1 (a); as grown, Sb_2S_3 (blue line) was deposited by evaporation and turned polycrystalline (red line) via annealing. See blue dash line; the absorption coefficient (above 600 nm) was like Si_3N_4, which has been widely used for all-dielectric metasurface in the visible spectrum for filter[34, 35], lasing cavity[36]. After the phase change, shown as the red dashed line, the absorption coefficient of c-Sb_2S_3 was also lossless above 700 nm. In Figure 1 (b), VO_2 was fabricated via sputter and underwent annealing. In addition, it was captured to tune the phase change property through a low phase change temperature. Such dynamic material has been used in smart windows[37, 38], sensor[39], cloak technology[40] and memristor[41]. However, it was unsuitable to design as all-VO_2 metasurface because of its high optical loss in the visible. Figure 1 (c) plots the optical constant of GST, which is taken from the reference[42]. GST have been often used in MIR as they have large absorption coefficients in visible wavelengths.

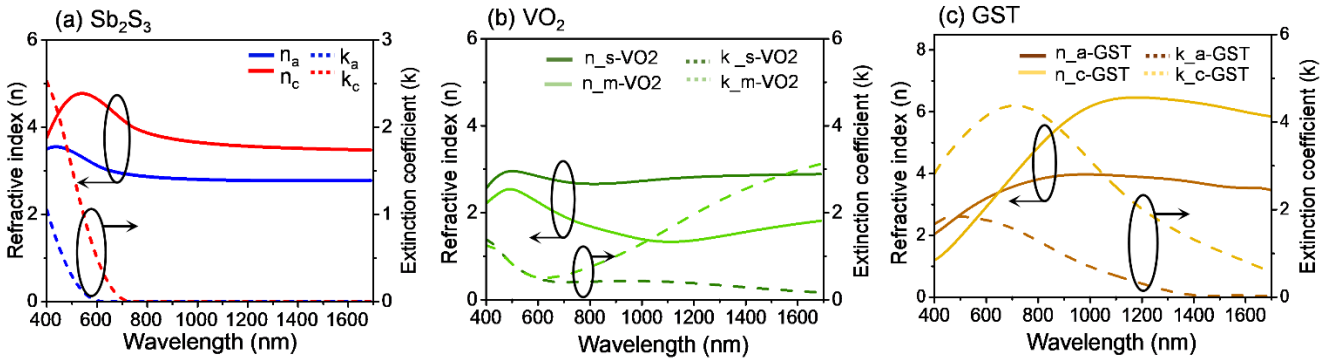

Figure 1. Optical constants of (a) Sb_2S_3 (b) VO_2, and (c) GST[42].

Phase change materials, including Sb_2S_3, VO_2, and GST, in the form of TPP devices, are discussed in Figure 2. VO_2 and GST have been exploited in photonic devices over 1.5 μm due to their intrinsic material loss in the visible spectrum. Although they were suggested near 1.1 μm, they were only used as a functional ultrathin layer[43-45]. Moreover, they were driven with DBR design in communication wavelength, and the thickness of DBR was thicker, which was inappropriate for modern quantum or optical devices. Therefore, Sb_2S_3 is suitable for reconfigurable designs in the metasurface or TPP in the NIR spectrum due to its lossless and large bandgap shift[25, 46]. The finite-difference time-domain (FDTD) method was used to calculate the phase change Tamm plasmon–polaritons (PC-TPP) resonance with normal light incidence at 600 nm to 1100 nm. In this modeling, the DBR has eight pairs of 145 nm silica and 95 nm TiO_2. The reflectance spectrum showing the DBR stop band is shown in grey area in Figure 2. In Figure 2 (a) and 2(b), the blue and red lines are the reflectance spectra of a- and c- Sb_2S_3 TPP, respectively, where the resonance wavelength shifted from 886 nm to 959 nm after the phase change process, resulting in a wavelength shift of 73 nm. Additionally, the mode characterization of shorter 741 nm resonance was discussed in Figure S7. In the modeling, the phase-change-material layer in each TPP case was set at the same thickness, 144 nm, with a 30-nm thick gold. It can be seen from Figure 2 (c) that conjugated the s-VO_2 with a metal layer, and PhC leads to low Q-factor TPP. Phase transition of the VO_2 from semiconductor to metal state leads to changing the phase matching condition for the TPP. As a result, the TPP wavelength shifts beyond the PhC band gap. In Figure 2 (d), the a- and c- GST (dark-brown and brown line, respectively) had no resonance dips.

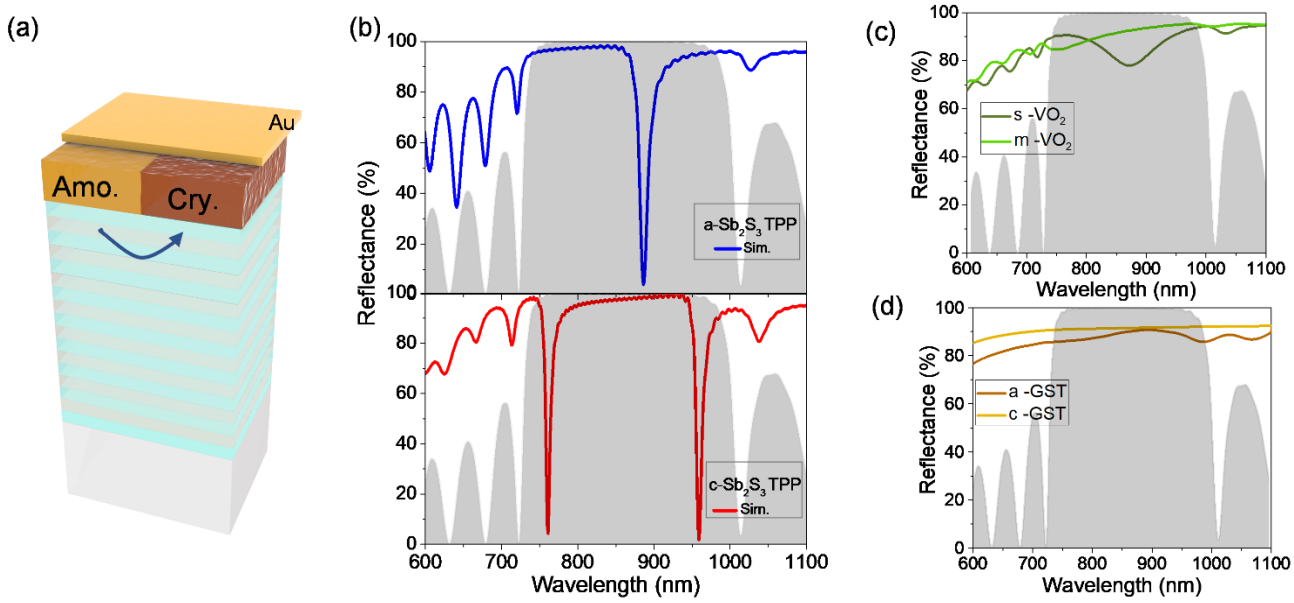

Figure 2. (a) Schematic of the TPP structure. Numerically simulated reflectance spectra of the Au-PCM-PhC structure with 144 nm PCM thickness for (b) a- and c-Sb_2S_3 TPP, (c) s- and m- VO_2 TPP, and (d) a- and c-GST TPP in the NIR.

The thickness-dependent spectrum of Sb_2S_3 TPP was simulated in Figure 3. In Figure 3 (a), the a-Sb_2S_3 TPP resonance was approximately 740 nm while c-Sb_2S_3 was around 780 nm with a thickness of 50 nm. As this thickness was greater than 150 nm, the TPP resonance of the amorphous and crystalline phases red-shifted, and they were at around 930 nm and 990 nm, respectively. At around 700 nm, the unexpected resonance was near the band edge of the DBR. In Figure 3(b), s-VO_2 and m-VO_2 TPP do not have a noticeable dip in the specific spectrum. In Figure 3 (c), neither had a clear resonance in the GST TPP case. Overall, compared to VO_2 and GST, Sb_2S_3 is a better candidate for manipulating the desired resonance with TPP in the NIR spectrum. Furthermore, it showed good development potential in the LiDAR area.

The dependence of the TPP wavelength on the PCM film thickness could be calculated analytically by solving the dispersion relations of TPP. A detailed description of the procedure for deriving the dispersion law for TPP was provided in the Supplementary Material. In general, the solution to the dispersion relations is a complex frequency. The real part of this complex frequency corresponds to the TPP wavelength inside the PhC band gap, while the imaginary part corresponds to the spectral width of the resonance line. The calculated real part of the complex frequency was presented in Figure 3 (a) in small circles. The results obtained by the TCMT and FDTD methods agree reasonably well. A slight difference near the edge of the PhC band gap was caused by the dispersion equation derived for a metal film combined with a semi-infinite PhC. In contrast, in the experiment, the number of the PhC periods was eight.

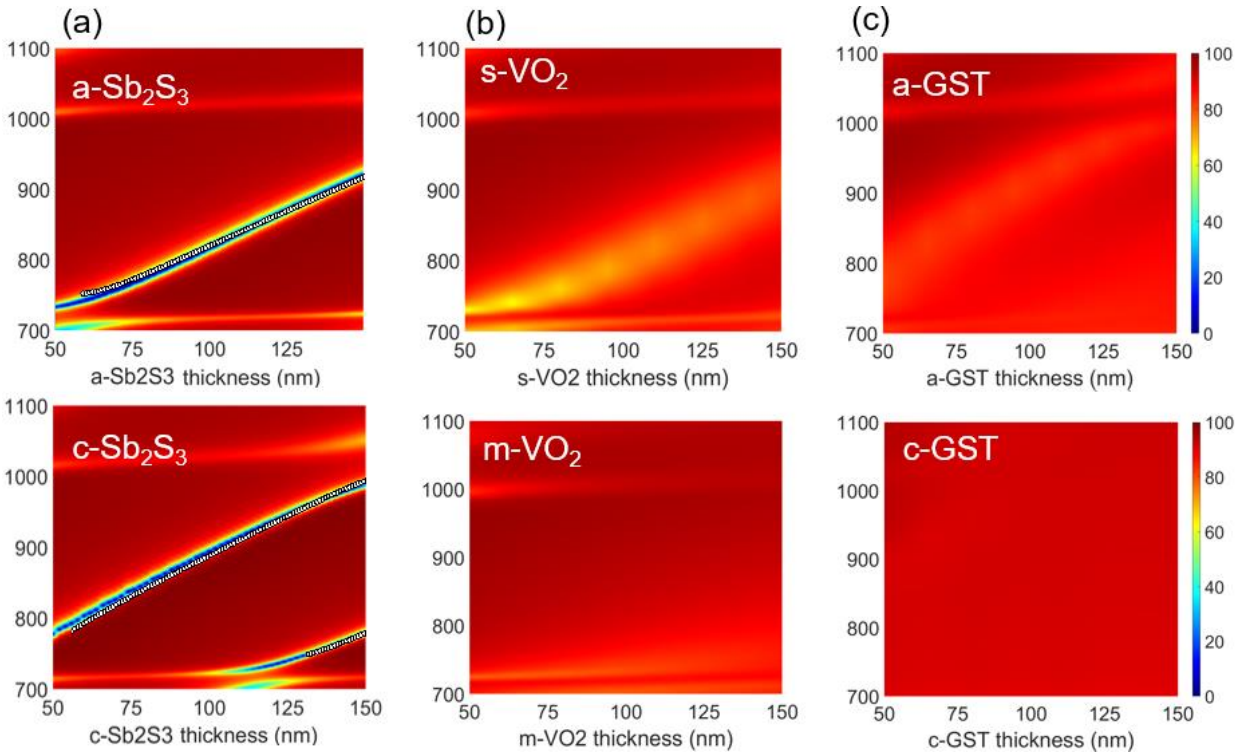

Figure 3. Simulated thickness-dependent spectra of Au-PC-PhC structures with (a) Sb_2S_3, (b) VO_2, and (c) GST as PCMs.

The optical bandgap was derived with the direct bandgap calculation through the Tauc equation by measuring the reflectance and transmittance of the films deposited on glass substrates. As shown in Figure 4 (a), the bandgap of a-Sb_2S_3 was 2.14 eV, and the curve feature shows a direct bandgap. In Figure 4 (b), the bandgap of c-Sb_2S_3 was shifted to 1.85 eV after the phase change process. Figures 4 (c) and (d) present the Raman spectra of the a- and c-Sb_2S_3, respectively. In the case of c-Sb_2S_3 case, the two major peaks, 282 and 301 cm^{-1}, correspond to the antisymmetric S-Sb-S stretching modes, and 147 cm^{-1} corresponds to the Sb metallic phase[25, 47, 48].

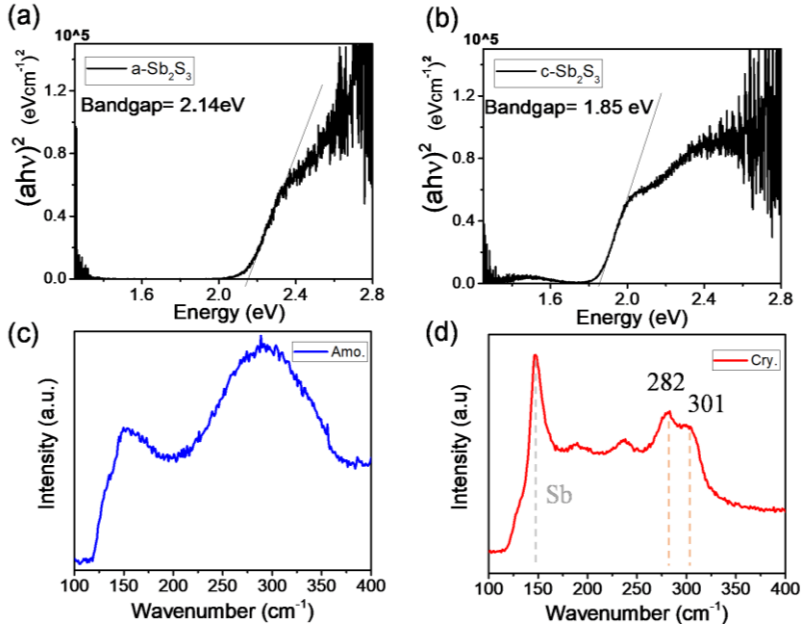

Figure 4. Tauc plots for (a) a-Sb_2S_3 and (b) c-Sb_2S_3. Optical bandgap energies were calculated with the Tauc function by measuring the reflectance and Transmittance of Sb_2S_3 on a glass. The Raman spectrum of (c) a-Sb_2S_3 and (d) c-Sb_2S_3. While a-Sb_2S_3 shows a broad bandwidth, c-Sb_2S_3 has two major peaks at 282 and 301 cm^{-1}. The metallic phase of Sb appears at 147 cm^{-1}.

Figure 5(a) shows the cross-section SEM image of the Sb_2S_3 TPP sample where periodic DBR multilayers are clearly shown. The experimental results of the Sb_2S_3 TPP sample achieved 45 nm wavelength shift from 886 nm to 932 nm after annealing the sample from amorphous (blue solid line) to crystal state (red solid line), as shown in Figure 5 (b). The experiment and simulation results were different because the annealing process could have resulted in the decrease of Sb_2S_3 films. The first reason was that the density of amorphous was 26% less than crystalline[49]. Secondly, we tested the annealing process in

the atmosphere and vacuum, resulting in oxidation and thinning, respectively. Hence, the Sb_2S_3 could be deposited with a few transparent dielectric layers (Al_2O_3 or Si_3N_4) to protect it within the phase change process in some research on the fabrication of the Sb_2S_3 metasurface[25, 46, 50]. In our Sb_2S_3 TPP case, the film thickness decreased around 30 nm after annealing. To avoid the thickness decrease of Sb_2S_3, the gold film was first deposited on a- Sb_2S_3 to maintain 128 nm c- Sb_2S_3 after the annealing.

The electric displacement field of the photonic device is shown in Figure 5 (c), and the most robust confinement was between Sb_2S_3 and gold film. In Figure 5 (d), the extensive refractive index modulation at the Sb_2S_3 shows that it has the HRI property compared to silicon in the NIR.

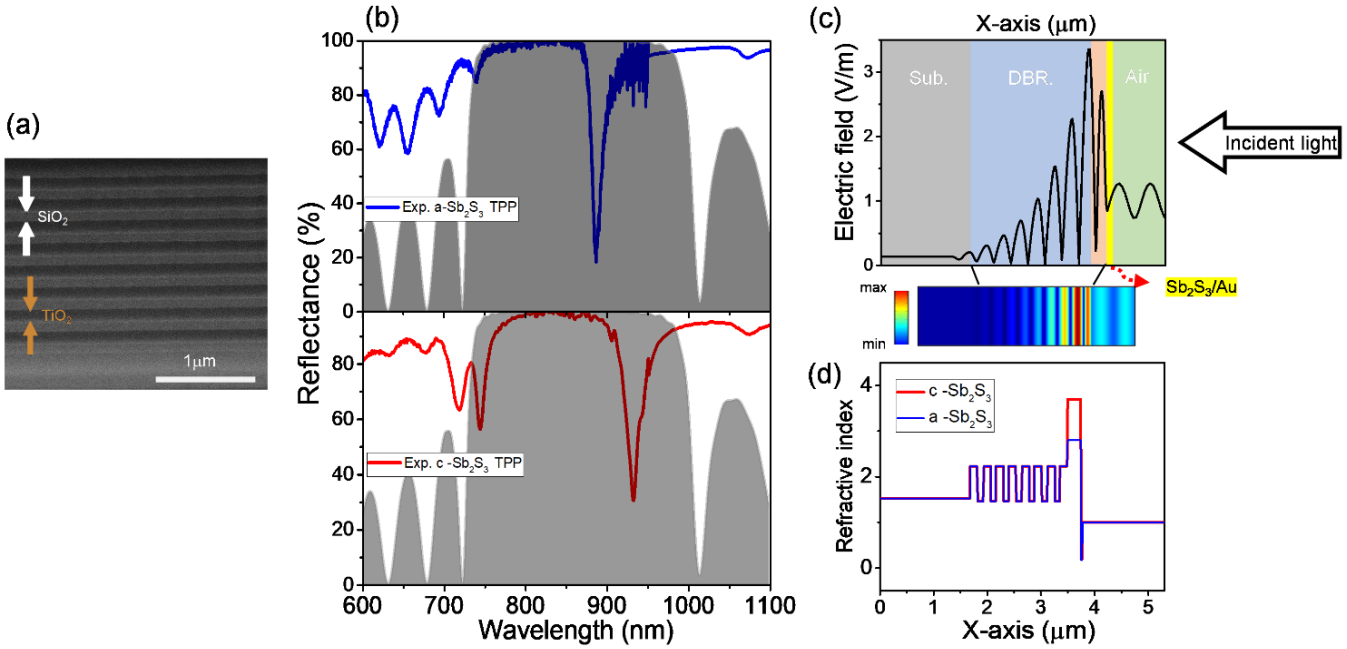

Figure 5. The experimental and E-field result of Sb_2S_3 TPP device. (a) SEM image. The SiO_2 and TiO_2 are shown in white and brown arrows, respectively. (b) The TPP resonance shifted from 886 nm to 932 by the phase change. (c) The electric field intensity profile of fundamental TPP mode with the incident light from air. (d) The refractive index profiles when the Sb_2S_3 is in amorphous and crystal phases.

In Figure 6 (a), angle-dependent reflectance was measured from 16° to 60° in the a-Sb_2S_3 PC-TPP case with a homemade system aiming for LiDAR application. The TPP resonance has a wavelength shift of 85 nm from 878 to 793 nm. The TPP resonance displayed a blue-shifted and slightly enhancing reflectance at larger oblique angles. It is consistent with the references that they theoretically computed transverse electric (TE) and transverse magnetic (TM) properties[51, 52]. However, while the wavelength variation of the experimental result fits well with the simulation, shown in Figure 6, we found that the dip was divided into two as the angles increased and started from 40°, the results were collected without a polarizer.

After the incident light was set as TE and TM mode, the results were manipulated by a-Sb_2S_3 TPP (details were shown in the Supplementary Information Figure S2). In TM mode, the reflectance results were kept within 8~12%, and the wavelength was from 873 nm to 797 nm (~76 nm shifted), while the angles were from 22° to 58°. In TE mode, the reflectance results changed from 13% to 40% when the wavelength was changed from 873 nm to 810 nm (~63 nm shifted). TE and TM were aligned through the same oblique angles with a starting wavelength of 873 nm, and the reflectance was almost the same at 12~13%. They had gradual varieties after the oblique angle was above 40° (847 nm). Meanwhile, the TM mode was moved to the blue-shift wavelength of 13 nm more than the TE mode. Furthermore, the spectrum of Figure S2 (c) derived from Figures S2 (a) and S2 (b) agreed with the trend of Figure 6. Hence, these results provided a new path for selective wavelength or intensity of signal applications in TE, TM, or unpolarized cases.

The c-Sb_2S_3 TPP device was also discussed in the Supplementary Information Figure S4. The results measured with an unpolarized light source also showed blue-shift and split peaks at large oblique angles. However, the reflectance and quality factor did not fit enough. The reason was that part of the Sb_2S_3 film on the last layer of DBR partially peeled off after the annealing progress of c-Sb_2S_3 TPP, which others hardly mentioned earlier. Hence, the Sb_2S_3 could be deposited with a few transparent dielectric layers (Al_2O_3 or Si_3N_4) to protect it within the phase change process in some research on the fabrication of the Sb_2S_3 metasurface[25, 46, 50].

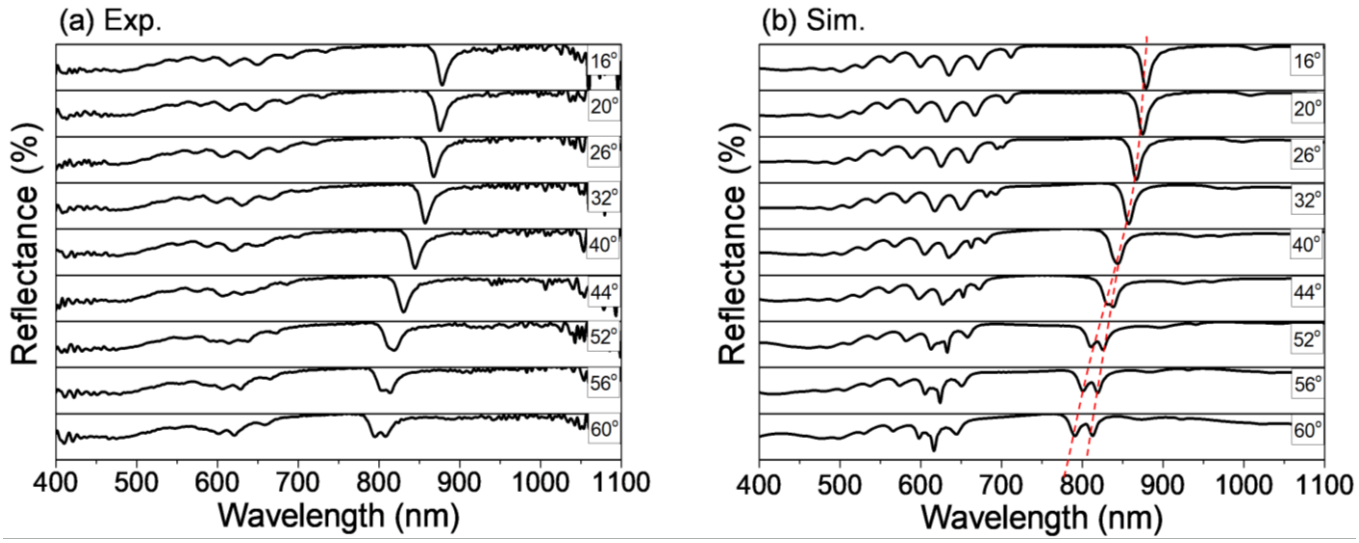

Figure 6. Un-polarized angle-dependent spectrum of a-Sb_2S_3 PC-TPP device (a) experiment and (b) simulation. (y-axis: max 100%, min 0%)

CONCLUSIONS

In conclusion, our work has shown that the lossless, high refractive index, and large refractive contrast properties of Sb_2S_3 are promising for versatile applications in NIR compared to other PCMs. With the current TPP design, the thickness of the Sb_2S_3 can be designed within this DBR stopband from 750 to 1000 nm. In the experiment, after phase transition, the resonance shift of 45 nm was demonstrated for the of Sb_2S_3 TPP from 886 nm to 932 nm. The main advantage of adopting Sb_2S_3 in this work, compared to other PCMs like VO_2 and GST, is an ultra-low extinction coefficient (~ 0) above 700 nm in both amorphous and crystalline states. This low optical loss ensures minimal energy dissipation and high-quality resonance in the visible to near-infrared (NIR) spectrum. In addition, the angle-dependent spectrum was systematically discussed in unpolarized, TE, and TM modes in simulation and experiment from 16° to 60°. The a-Sb_2S_3 PC-TPP resonance has a significant wavelength shift of 85 nm (from 878 to 793 nm). This is the largest wavelength modulation in TPP devices reported so far. For the returning process from crystalline to amorphous state, it could be realized by femto-second laser[25] or electrical short pulse quenching[46]. However, damaging the metal films should be avoided. With this regard, the refractory plasmonic materials could be considered[53, 54].

This research provides an essential guideline for studying high-Q adjustable 1D-photonic with lossless and high refractive index, phase change materials. The potential applications of the work include optical memory, optical data storage, and LiDAR receiver systems.

EXPERIMENTAL SECTION

To fabricate the Sb_2S_3 TPP device, the DBR layers (SiO_2 and TiO_2) were first fabricated via E-beam evaporation. Gold film and Sb_2S_3 were also deposited on the DBR through E-beam evaporation. The gold/a-Sb_2S_3/DBR sample was annealed at 250 °C for two hours in a vacuum furnace at a rate of 0.15 °C/sec to become the gold/c-Sb_2S_3/DBR sample.

The refractive index and extinction coefficient were collected by a spectroscopic ellipsometer (J. A. Woollam). Raman spectra were measured by a WITec alpha300 (WITec, GmbH, Germany) with a 532 nm CW laser. The reflectance and transmittance spectra were collected by an optical microscope (BX51, Olympus) with a 20× objective lens (NA = 0.4) and passed through two spectrum sensors (SE2020-025-FUV, SW2540) to cover a wide spectral range. The angle-dependent spectrum was measured by a homemade angle-dependent measurement system.

Corresponding Author

*E-mail: kpchen@ee.nthu.edu.tw

Notes.

The authors declare no competing financial interest.

ACKNOWLEDGMENT

This work is supported by the National Science and Technology Council (NSTC; 111-2923-E-007-008-MY3; 111-2628-E-007-021; 112-2223-E-007 -007 -MY3; 112-2923-E-007 -004 -MY2; 112-2119-M-A49-008). This research was also funded by the Russian Science Foundation (project no. 22-42-08003).

Uncategorized References

1. Soref, R., Mid-infrared photonics in silicon and germanium. *Nature photonics* **2010,** *4* (8), 495-497.
2. Chaisakul, P.; Marris-Morini, D.; Frigerio, J.; Chrastina, D.; Rouifed, M.-S.; Cecchi, S.; Crozat, P.; Isella, G.; Vivien, L., Integrated germanium optical interconnects on silicon substrates. *Nature Photonics* **2014,** *8* (6), 482-488.
3. Kim, D. U.; Park, Y. J.; Kim, D. Y.; Jeong, Y.; Lim, M. G.; Hong, M. S.; Her, M. J.; Rah, Y.; Choi, D. J.; Han, S., Programmable photonic arrays based on microelectromechanical elements with femtowatt-level standby power consumption. *Nature Photonics* **2023,** *17* (12), 1089-1096.
4. Uematsu, T.; Ishizaka, Y.; Kawaguchi, Y.; Saitoh, K.; Koshiba, M., Design of a compact two-mode multi/demultiplexer consisting of multimode interference waveguides and a wavelength-insensitive phase shifter for mode-division multiplexing transmission. *Journal of Lightwave Technology* **2012,** *30* (15), 2421-2426.
5. Reed, G. T.; Mashanovich, G.; Gardes, F. Y.; Thomson, D., Silicon optical modulators. *Nature photonics* **2010,** *4* (8), 518-526.
6. Rahim, A.; Hermans, A.; Wohlfeil, B.; Petousi, D.; Kuyken, B.; Van Thourhout, D.; Baets, R., Taking silicon photonics modulators to a higher performance level: state-of-the-art and a review of new technologies. *Advanced Photonics* **2021,** *3* (2), 024003-024003.
7. Shen, B.; Wang, P.; Polson, R.; Menon, R., An integrated-nanophotonics polarization beamsplitter with 2.4× 2.4 μm2 footprint. *Nature Photonics* **2015,** *9* (6), 378-382.
8. Dai, D.; Wang, Z.; Peters, J.; Bowers, J. E., Compact polarization beam splitter using an asymmetrical Mach–Zehnder interferometer based on silicon-on-insulator waveguides. *IEEE Photonics Technology Letters* **2012,** *24* (8), 673-675.
9. Liu, D.; He, J.; Zhu, M.; Xiang, Y.; Zhang, L.; Zhang, M.; Xu, Y.; Dai, D., High-Performance Silicon Photonic Filter Using Subwavelength-Structure Multimode Waveguide Gratings. *Laser & Photonics Reviews* **2023,** *17* (12), 2300485.
10. Shu, H.; Chang, L.; Tao, Y.; Shen, B.; Xie, W.; Jin, M.; Netherton, A.; Tao, Z.; Zhang, X.; Chen, R., Microcomb-driven silicon photonic systems. *Nature* **2022,** *605* (7910), 457-463.
11. Grajower, M.; Mazurski, N.; Shappir, J.; Levy, U., Non-Volatile Silicon Photonics Using Nanoscale Flash Memory Technology. *Laser & Photonics Reviews* **2018,** *12* (4), 1700190.
12. Wang, J.; Paesani, S.; Ding, Y.; Santagati, R.; Skrzypczyk, P.; Salavrakos, A.; Tura, J.; Augusiak, R.; Mančinska, L.; Bacco, D., Multidimensional quantum entanglement with large-scale integrated optics. *Science* **2018,** *360* (6386), 285-291.
13. Wan, N. H.; Lu, T.-J.; Chen, K. C.; Walsh, M. P.; Trusheim, M. E.; De Santis, L.; Bersin, E. A.; Harris, I. B.; Mouradian, S. L.; Christen, I. R., Large-scale integration of artificial atoms in hybrid photonic circuits. *Nature* **2020,** *583* (7815), 226-231.
14. Lee, M.; Fauchet, P. M., Two-dimensional silicon photonic crystal based biosensing platform for protein detection. *Optics express* **2007,** *15* (8), 4530-4535.
15. Wang, J.; Sanchez, M. M.; Yin, Y.; Herzer, R.; Ma, L.; Schmidt, O. G., Silicon-based integrated label-free optofluidic biosensors: latest advances and roadmap. *Advanced Materials Technologies* **2020,** *5* (6), 1901138.
16. Quack, N.; Takabayashi, A. Y.; Sattari, H.; Edinger, P.; Jo, G.; Bleiker, S. J.; Errando-Herranz, C.; Gylfason, K. B.; Niklaus, F.; Khan, U., Integrated silicon photonic MEMS. *Microsystems & Nanoengineering* **2023,** *9* (1), 27.
17. Bogaerts, W.; Pérez, D.; Capmany, J.; Miller, D. A.; Poon, J.; Englund, D.; Morichetti, F.; Melloni, A., Programmable photonic circuits. *Nature* **2020,** *586* (7828), 207-216.
18. Park, J.; Jeong, B. G.; Kim, S. I.; Lee, D.; Kim, J.; Shin, C.; Lee, C. B.; Otsuka, T.; Kyoung, J.; Kim, S., All-solid-state spatial light modulator with independent phase and amplitude control for three-dimensional LiDAR applications. *Nature nanotechnology* **2021,** *16* (1), 69-76.

19. Huang, Y.-W.; Lee, H. W. H.; Sokhoyan, R.; Pala, R. A.; Thyagarajan, K.; Han, S.; Tsai, D. P.; Atwater, H. A., Gate-tunable conducting oxide metasurfaces. *Nano letters* **2016,** *16* (9), 5319-5325.
20. Kaliteevski, M.; Iorsh, I.; Brand, S.; Abram, R.; Chamberlain, J.; Kavokin, A.; Shelykh, I., Tamm plasmon-polaritons: Possible electromagnetic states at the interface of a metal and a dielectric Bragg mirror. *Physical Review B* **2007,** *76* (16), 165415.
21. Wu, B. R.; Yang, J. H.; Pankin, P. S.; Huang, C. H.; Lee, W.; Maksimov, D. N.; Timofeev, I. V.; Chen, K. P., Quasi-Bound States in the Continuum with Temperature-Tunable Q Factors and Critical Coupling Point at Brewster's Angle. *Laser & Photonics Reviews* **2021,** *15* (5), 2000290.
22. Nakamura, K.; Narumi, K.; Kikuchi, K.; Inada, Y. In *Liquid crystal-tunable optical phased array for LiDAR applications*, Smart Photonic and Optoelectronic Integrated Circuits XXIII, SPIE: 2021; pp 94-99.
23. Kim, I.; Martins, R. J.; Jang, J.; Badloe, T.; Khadir, S.; Jung, H.-Y.; Kim, H.; Kim, J.; Genevet, P.; Rho, J., Nanophotonics for light detection and ranging technology. *Nature nanotechnology* **2021,** *16* (5), 508-524.
24. Zhang, Y.; Fowler, C.; Liang, J.; Azhar, B.; Shalaginov, M. Y.; Deckoff-Jones, S.; An, S.; Chou, J. B.; Roberts, C. M.; Liberman, V., Electrically reconfigurable non-volatile metasurface using low-loss optical phase-change material. *Nature Nanotechnology* **2021,** *16* (6), 661-666.
25. Lu, L.; Dong, Z.; Tijiptoharsono, F.; Ng, R. J. H.; Wang, H.; Rezaei, S. D.; Wang, Y.; Leong, H. S.; Lim, P. C.; Yang, J. K., Reversible tuning of Mie resonances in the visible spectrum. *ACS nano* **2021,** *15* (12), 19722-19732.
26. Liu, H.; Dong, W.; Wang, H.; Lu, L.; Ruan, Q.; Tan, Y. S.; Simpson, R. E.; Yang, J. K., Rewritable color nanoprints in antimony trisulfide films. *Science advances* **2020,** *6* (51), eabb7171.
27. Yoon, H.; Choi, M.; Lim, T.-W.; Kwon, H.; Ihm, K.; Kim, J. K.; Choi, S.-Y.; Son, J., Reversible phase modulation and hydrogen storage in multivalent VO2 epitaxial thin films. *Nature materials* **2016,** *15* (10), 1113-1119.
28. Howes, A.; Zhu, Z.; Curie, D.; Avila, J. R.; Wheeler, V. D.; Haglund, R. F.; Valentine, J. G., Optical limiting based on Huygens' metasurfaces. *Nano Letters* **2020,** *20* (6), 4638-4644.
29. Dong, W.; Liu, H.; Behera, J. K.; Lu, L.; Ng, R. J.; Sreekanth, K. V.; Zhou, X.; Yang, J. K.; Simpson, R. E., Wide bandgap phase change material tuned visible photonics. *Advanced Functional Materials* **2019,** *29* (6), 1806181.
30. Sreekanth, K. V.; Perumal, J.; Dinish, U.; Prabhathan, P.; Liu, Y.; Singh, R.; Olivo, M.; Teng, J., Tunable Tamm plasmon cavity as a scalable biosensing platform for surface enhanced resonance Raman spectroscopy. *Nature Communications* **2023,** *14* (1), 7085.
31. De Galarreta, C. R.; Alexeev, A. M.; Au, Y. Y.; Lopez-Garcia, M.; Klemm, M.; Cryan, M.; Bertolotti, J.; Wright, C. D., Nonvolatile reconfigurable phase-change metadevices for beam steering in the near infrared. *Advanced Functional Materials* **2018,** *28* (10), 1704993.
32. Wurdack, M.; Lundt, N.; Klaas, M.; Baumann, V.; Kavokin, A. V.; Höfling, S.; Schneider, C., Observation of hybrid Tamm-plasmon exciton-polaritons with GaAs quantum wells and a MoSe2 monolayer. *Nature communications* **2017,** *8* (1), 1-6.
33. Leuthold, J.; Dorodnyy, A., On-demand emission from Tamm plasmons. *Nature Materials* **2021,** *20* (12), 1595-1596.
34. Yang, J.-H.; Babicheva, V. E.; Yu, M.-W.; Lu, T.-C.; Lin, T.-R.; Chen, K.-P., Structural colors enabled by lattice resonance on silicon nitride metasurfaces. *ACS nano* **2020,** *14* (5), 5678-5685.
35. Wang, J.; Yu, F.; Chen, J.; Wang, J.; Chen, R.; Zhao, Z.; Chen, J.; Chen, X.; Lu, W.; Li, G., Continuous-Spectrum–Polarization Recombinant Optical Encryption with a Dielectric Metasurface. *Advanced Materials* **2023,** *35* (41), 2304161.
36. Yang, J. H.; Huang, Z. T.; Maksimov, D. N.; Pankin, P. S.; Timofeev, I. V.; Hong, K. B.; Li, H.; Chen, J. W.; Hsu, C. Y.; Liu, Y. Y., Low-threshold bound state in the continuum lasers in hybrid lattice resonance metasurfaces. *Laser & Photonics Reviews* **2021,** *15* (10), 2100118.
37. Cui, Y.; Ke, Y.; Liu, C.; Chen, Z.; Wang, N.; Zhang, L.; Zhou, Y.; Wang, S.; Gao, Y.; Long, Y., Thermochromic VO2 for energy-efficient smart windows. *Joule* **2018,** *2* (9), 1707-1746.

38. Li, M.; Magdassi, S.; Gao, Y.; Long, Y., Hydrothermal synthesis of VO2 polymorphs: advantages, challenges and prospects for the application of energy efficient smart windows. *small* **2017,** *13* (36), 1701147.
39. Li, G.; Xie, D.; Zhang, Z.; Zhou, Q.; Zhong, H.; Ni, H.; Wang, J.; Guo, E. j.; He, M.; Wang, C., Flexible VO2 Films for In-Sensor Computing with Ultraviolet Light. *Advanced Functional Materials* **2022,** *32* (29), 2203074.
40. Xiao, L.; Ma, H.; Liu, J.; Zhao, W.; Jia, Y.; Zhao, Q.; Liu, K.; Wu, Y.; Wei, Y.; Fan, S., Fast adaptive thermal camouflage based on flexible VO2/graphene/CNT thin films. *Nano letters* **2015,** *15* (12), 8365-8370.
41. Yi, W.; Tsang, K. K.; Lam, S. K.; Bai, X.; Crowell, J. A.; Flores, E. A., Biological plausibility and stochasticity in scalable VO2 active memristor neurons. *Nature communications* **2018,** *9* (1), 4661.
42. Zhu, M.; Abdollahramezani, S.; Li, C.; Fan, T.; Harutyunyan, H.; Adibi, A., Dynamically tunable second-harmonic generation using hybrid nanostructures incorporating phase-change chalcogenides. *Nanophotonics* **2022,** *11* (11), 2727-2735.
43. Tripathi, A.; John, J.; Kruk, S.; Zhang, Z.; Nguyen, H. S.; Berguiga, L.; Romeo, P. R.; Orobtchouk, R.; Ramanathan, S.; Kivshar, Y., Tunable Mie-resonant dielectric metasurfaces based on VO2 phase-transition materials. *ACS photonics* **2021,** *8* (4), 1206-1213.
44. Long, L.; Taylor, S.; Wang, L., Enhanced infrared emission by thermally switching the excitation of magnetic polariton with scalable microstructured VO2 metasurfaces. *ACS Photonics* **2020,** *7* (8), 2219-2227.
45. Abdollahramezani, S.; Hemmatyar, O.; Taghinejad, M.; Taghinejad, H.; Kiarashinejad, Y.; Zandehshahvar, M.; Fan, T.; Deshmukh, S.; Eftekhar, A. A.; Cai, W., Dynamic hybrid metasurfaces. *Nano letters* **2021,** *21* (3), 1238-1245.
46. Chen, R.; Fang, Z.; Perez, C.; Miller, F.; Kumari, K.; Saxena, A.; Zheng, J.; Geiger, S. J.; Goodson, K. E.; Majumdar, A., Non-volatile electrically programmable integrated photonics with a 5-bit operation. *Nature Communications* **2023,** *14* (1), 3465.
47. Delaney, M.; Zeimpekis, I.; Lawson, D.; Hewak, D. W.; Muskens, O. L., A new family of ultralow loss reversible phase-change materials for photonic integrated circuits: Sb2S3 and Sb2Se3. *Advanced Functional Materials* **2020,** *30* (36), 2002447.
48. Parize, R.; Cossuet, T.; Chaix-Pluchery, O.; Roussel, H.; Appert, E.; Consonni, V., In situ analysis of the crystallization process of Sb2S3 thin films by Raman scattering and X-ray diffraction. *Materials & Design* **2017,** *121*, 1-10.
49. Kaito, C.; Nakamura, N.; Yoshida, T.; Shiojiri, M., Structure and the process of crystallization in thin amorphous Sb2S3 films. *Journal of crystal growth* **1984,** *66* (1), 156-162.
50. Liu, T.; Han, Z.; Duan, J.; Xiao, S., Phase-change metasurfaces for dynamic image display and information encryption. *Physical Review Applied* **2022,** *18* (4), 044078.
51. Kaliteevski, M.; Iorsh, I.; Brand, S.; Abram, R.; Chamberlain, J.; Kavokin, A.; Shelykh, I., Tamm plasmon-polaritons: Possible electromagnetic states at the interface of a metal and a dielectric Bragg mirror. *Physical Review B—Condensed Matter and Materials Physics* **2007,** *76* (16), 165415.
52. Lu, H.; Gan, X.; Mao, D.; Fan, Y.; Yang, D.; Zhao, J., Nearly perfect absorption of light in monolayer molybdenum disulfide supported by multilayer structures. *Optics express* **2017,** *25* (18), 21630-21636.
53. Guler, U.; Boltasseva, A.; Shalaev, V. M., Refractory plasmonics. *Science* **2014,** *344* (6181), 263-264.
54. Yang, Z. Y.; Ishii, S.; Doan, A. T.; Shinde, S. L.; Dao, T. D.; Lo, Y. P.; Chen, K. P.; Nagao, T., Narrow-band thermal emitter with titanium nitride thin film demonstrating high temperature stability. *Advanced Optical Materials* **2020,** *8* (8), 1900982.